

Solving the twin image problem in in-line holography by using multiple defocused intensity images reconstructed from a single hologram

Marius Ipo Gnetto, Yao Taky Alvarez Kossonou, Yao Koffi, Kenneth A. Kaduki & Jérémie T. Zoueu

To cite this article: Marius Ipo Gnetto, Yao Taky Alvarez Kossonou, Yao Koffi, Kenneth A. Kaduki & Jérémie T. Zoueu (2022) Solving the twin image problem in in-line holography by using multiple defocused intensity images reconstructed from a single hologram, Journal of Modern Optics, 69:3, 121-129, DOI: [10.1080/09500340.2021.2011450](https://doi.org/10.1080/09500340.2021.2011450)

To link to this article: <https://doi.org/10.1080/09500340.2021.2011450>



Published online: 14 Dec 2021.



Submit your article to this journal [↗](#)



Article views: 331



View related articles [↗](#)



View Crossmark data [↗](#)



Citing articles: 1 View citing articles [↗](#)



Solving the twin image problem in in-line holography by using multiple defocused intensity images reconstructed from a single hologram

Marius Ipo Gnetto^{a,b}, Yao Taky Alvarez Kossonou^a, Yao Koffi^a, Kenneth A. Kaduki^b and Jérémie T. Zoueu^a

^aLaboratoire d'Instrumentation, Image et Spectroscopie (L2IS), Institut National Polytechnique Felix Houphouët-Boigny (INPHB), Yamoussoukro, Côte d'Ivoire; ^bDepartment of Physics, University of Nairobi, Nairobi, Kenya

ABSTRACT

Phase recovery from a hologram measurement is at the heart of coherent imaging techniques and online holography. In-line holography suffers from a blurred background problem that results from double images formed during hologram reconstruction. This so-called double image problem, inherent to the in-line geometry of the holographic experimental setup, limits the quality of the information (shape or refractive index of the object) obtained by reconstruction algorithms using a single hologram. We propose here a numerical reconstruction method combining the angular spectrum method (ASM) and the transport of intensity equation method using Gaussian process regression (GP-TIE) to solve this problem. In our approach, a single in-line hologram is used to recover the phase image free of any perturbation due to the presence of the double image.

ARTICLE HISTORY

Received 15 March 2021

Accepted 22 November 2021

KEYWORDS

In-line digital holography; defocused intensity images; phase image reconstruction technique; computational imaging

1. Introduction

The phase contains information about an optical field that can often be related to the surface profile and refractive index of an object [1]. This information is therefore essential in studies of transparent samples, regardless of the imaging system used. In-line holography is an imaging system in which, recovering the phase is more than necessary to separate not only the artefacts linked to the presence of the twin image due to the geometry of the experimental device but also those produced by cross interference from neighbouring parts of the sample. Phase problems are traditionally solved for the most part, by approaches based on the method developed by Gerchberg-Saxton [2]. Most of these methods use multiple holograms acquired by scanning object-detector distance and require a certain object's surrounding or so-called support, to accurately recover phase information lost during the recording step, based on an iterative solution [3–14].

An alternative to Gerchberg-Saxton-based approaches is the Transport of intensity equation (TIE) technique [15–25]. This method offers a simple technique for calculating the phase quantitatively from several images of defocused intensities [1]. Focus intensity images contain no phase information; however, defocus introduces phase contrast [17]. However, in most techniques using TIE,

the acquisition of intensity images requires a 4-f imaging system [26]. With such an imaging system, the camera or sample would have to be moved along the axis of light propagation, creating registration problems on the acquired intensity images. To solve this problem, Waller et al. [27], used a multiplexed volume hologram to simultaneously produce images at different distances from the camera. Zuo et al. [28] later used a lens at the pupillary plane of the 4-f system to modify the position of the image plane. These two techniques are based on a 4-f imaging system and use optical elements to change planes (object or image). Recently, Zhou et al. [29] have proposed an approach that does not use any optical part to generate the intensity images used by TIE to recover phase. However, their method requires the capture of two images that are defocused from each other to recover the phase. When more than two defocused images in an axial stack are used, the linearity assumption inherent in the TIE technique may no longer be valid [1], which constitutes a major limitation of TIE. Also, the effect of the twin image was not studied in this work.

We propose a technique in which a single hologram acquired by an in-line holographic device is needed to recover the phase. We start by using the angular spectrum method to reconstruct, from a single in-line hologram

and at different focusing distances, a stack (dataset) of intensity images. In this dataset, all reconstructed images are stacked in a column ready for input into a GP-TIE algorithm similar to the one developed by Zhong et al. [17] in optical microscopy to recover the phase of biological samples with a small phase variation. The algorithm uses Gaussian regression to estimate the axial derivative of intensity used to recover the phase. Thus, by using a single hologram to recover the phase, we free ourselves not only from the need to use several holograms and support constraints to recover the phase as in most iterative methods of phase reconstruction in in-line holography. Finally, the use of the GP-TIE method allowed us to solve the linearity problem inherent in the TIE method.

2. Materials

2.1. Experimental set up

Figure 1 shows the configuration of the in-line digital hologram recording device. This is made up of a laser (He-Ne) with a wavelength of 633 nm and a maximum output power of 1 mW. A pinhole with a diameter of 10 μm , constituting our source point and located at 6 mm (z_1) from the sample, allows for a field of view wide enough to cover the entire volume of the sample. A monochrome CMOS DMK 37BUX178 camera with a USB 3.1 interface has 3072×2048 pixels and a pixel size of 2.4 μm . The detector is located at a distance $z_2 = 40\text{mm}$ from the source point. Its role is to capture the intensity image resulting from the interference between the reference wave and the wave diffracted by the sample then the computer connected to the camera by a USB 3.1 cable, records the hologram.

2.2. Preparation of the sample

In this work, a carboxylate microbead 10 μm in diameter and refractive index $n = 1.5867$ was used as the sample. A small drop of the microbead solution, diluted with distilled water, was placed, and spread on a standard glass coverslip of size 76 mm \times 26 mm \times 1 mm and allowed to dry for about 30 min. The sample was prepared at 25°C.

2.3. Hologram normalization

Prior to the reconstruction procedure, the hologram is normalized to eliminate effects of background imperfections. The background image is recorded under the same experimental conditions as the hologram [30]. The procedure was as follows:

- (i) The reference image (I_R) was recorded using an empty slide. The recording was done the source illumination turned on.
- (ii) The image of the hologram (I_H) was recorded using the slide containing the sample.
- (iii) Normalization of the hologram is done by dividing the hologram image by the background image. The normalized image is called I_N .

The normalization operation of the hologram is expressed by the following equation:

$$I_N = I_H / I_R \quad (1)$$

This normalized image was used as input to the angular spectrum reconstruction algorithm.

3. Method

3.1. Angular spectrum method (ASM)

The angular spectrum propagation method is based on the principle of plane wave decomposition. It consists of decomposing the wave in the plane of the hologram into a sum of plane waves and propagating these plane waves in the space of spatial frequencies. Thus, reconstruction by the angular spectrum causes the plane waves to propagate individually through multiplication by a phase term called the optical transfer function $H(f_x, f_y, z)$. It characterizes the propagation in frequency space which acts as a linear system [31]. In our work, we have used the Fresnel transfer function in the vacuum to digitally back-propagate the field to multiple planes in the volume of interest. At each step, the Fourier transform of the hologram is multiplied by the Fresnel transfer function at a

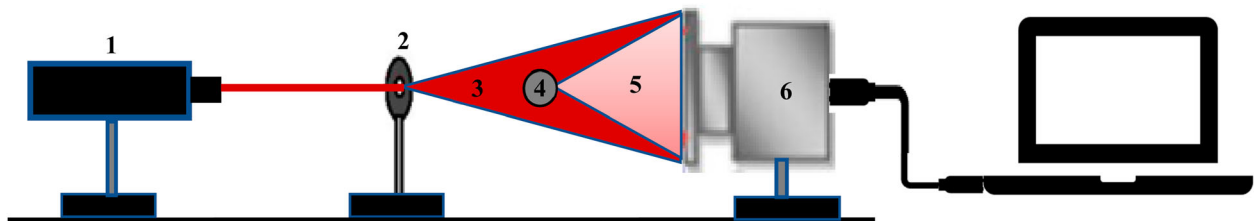


Figure 1. Schematic of the in-line digital hologram recording device: (1) laser; (2) pinhole; (3) reference wave; (4) sample; (5) wave diffracted by the object; (6) camera; (7) computer.

given distance to find the spectral components at this distance from the sensor plane. Then, an inverse Fourier transform is applied to reconstruct the object field in the spatial domain from the computed spectra. The Fresnel approximated transfer function is defined below:

$$H(f_x, f_y, z) = e^{jkz} \exp[j\pi \lambda z (f_x^2 + f_y^2)] \quad (2)$$

where k is the wave number, which is equal to $\frac{2\pi}{\lambda}$ in vacuum, z is the distance between the object plane and the hologram plane, (f_x, f_y) are the coordinates in frequency space.

The reconstructed field $\psi(x, y, z)$ is given by:

$$\psi(x, y, z) = \text{FT}^{-1}[\text{FT}[\psi_0(x_0, y_0)] * H(f_x, f_y, z)] \quad (3)$$

FT and FT^{-1} are the Fourier transform and the inverse Fourier transform respectively, $\psi_0(x_0, y_0)$ and $\psi(x, y, z)$ are the complex distributions of wave fields in the object plane and in the hologram plane respectively and $H(f_x, f_y, z)$ is the Fresnel transfer function in vacuum. With this method, the size of the intensity of the reconstructed images does not change when the reconstruction distances change [8]. This ensures correct recording of the image over the entire reconstruction depth [29]. The intensity images reconstructed at different planes are obtained using the following equation:

$$I(x, y, z) = |\psi(x, y, z)|^2 \quad (4)$$

In 2015, Tatiana et al. [31] established a relationship between holograms recorded with plane and spherical waves respectively that implies that a hologram recorded with a spherical wave can be reconstructed as it was recorded with plane waves, or vice versa. We have considered this relationship in the algorithm of reconstruction of intensity images to consider the effects of spherical aberration that induce blurring on the edges of the image. The following equation defines this relationship:

$$S_{\text{plane}} = \frac{z_1}{z_2} S_{\text{spherical}} \quad (5)$$

where z_1 and z_2 are respectively the distance from the object to the detector and the distance from the pinhole to the detector, S_{plane} and $S_{\text{spherical}}$ are respectively the surfaces of the holograms recorded with plane and spherical waves. We have introduced a numerical method based on the Sobel gradient, to automatically determine the optimal position of the focal plane in the digital reconstruction. This algorithm used is the same as that used in [32]. The focusing measure F of a given image $I(m, n)$ defined as in [33] is introduced as a variance of Sobel

gradient magnitudes defined by the following equation:

$$F(I) = \frac{1}{NM} * \sum_n^N \sum_m^M (\nabla S(m, n) - \overline{\nabla S})^2 \quad (6)$$

The gradient magnitudes for each image of reconstructed intensity $I(m, n)$ are calculated from the gradients along the horizontal and vertical axes ∇S_x and ∇S_y using the following equation:

$$\nabla S(m, n) = \sqrt{\nabla S_x(m, n)^2 + \nabla S_y(m, n)^2} \quad (7)$$

With ∇S_x and ∇S_y obtained by convolving the input image $I(m, n)$ with the operators Sobel defines as follows:

$$S_x = \begin{pmatrix} -1 & 0 & 1 \\ -2 & 0 & 2 \\ -1 & 0 & 1 \end{pmatrix} \text{ and } S_y = \begin{pmatrix} 1 & 2 & 1 \\ 0 & 0 & 0 \\ -1 & -2 & -1 \end{pmatrix} \quad (8)$$

As input, the autofocus algorithm requires an approximate interval a few millimetres wide containing the correct reconstruction distance from the object plane. This reconstruction distance can be determined, subject to the Nyquist criterion, by the following equation [34]:

$$L_{\text{rmin}} = N * \text{Ps} \left[\left(\frac{\text{Ps}}{2\lambda} \right)^2 - 1 \right]^{1/2} \approx \frac{N * (\text{Ps})^2}{2\lambda} \quad (9)$$

where N is the number of pixels on a row of the detector; Ps is the pixel size of the detector and λ is the wavelength of the illumination source. To use this dataset of reconstructed intensity images in the GP-TIE method that we will describe in the next section, we stack these images vertically. The position of each reconstructed intensity image forms a column vector which will be defined by a parameter in the GP-TIE algorithm.

3.2. The GP-TIE approach

When a wave field passes through an object, the intensity distribution recorded by the detector is modulated by the profile of the phase distribution of the object. Therefore, the phase information can be retrieved from the intensity image using the TIE technique. Let $I(x, y, z)$ be the intensity distribution at the image plane and $\phi(x, y, z)$ be the corresponding phase distribution. TIE is defined as follows [15]:

$$\nabla(I(x, y, z) \nabla \phi(x, y, z)) = -\frac{2\pi}{\lambda} \frac{\partial I(x, y, z)}{\partial z} \quad (10)$$

where ∇ is the 2D transverse gradient operator, λ is the wavelength and $\partial/\partial z$ is the axial derivative along z . The numerical solution of Equation (9) in the case of a phase

object (transparent object), is given by Equation (10), resulting from the standard Poisson equation [20].

$$\phi(x, y, z) = \text{FT}^{-1} \left[\frac{\text{FT} \left[-\frac{2\pi}{\lambda} \frac{1}{I(x, y, z)} \frac{\partial I(x, y, z)}{\partial z} \right]}{4\pi^2(f_x^2 + f_y^2)} \right] \quad (11)$$

where FT and FT^{-1} denote, respectively, the Fourier transform and the inverse Fourier transform and (f_x, f_y) denotes the spatial frequency variables corresponding to the coordinates (x, y) . Finding the distribution of the phase of the wave field amounts to giving a precise estimate of $\frac{\partial I(x, y, z)}{\partial z}$ because the phase of the wave field is related to the variation of the intensity of the image along the optical axis. In this work, we used the method proposed by Zhong et al. [17] to accurately estimate the axial derivative of the intensity. This method performs an adjustment (by Gaussian regression) on the intensity of each pixel in the frequency domain along the optical axis, considering all the images in different planes. Gaussian regression computes a weighted average of the noisy observations y as $\hat{f}(X_*) = k(X_*)^T (K + \sigma_n^2 I)^{-1} y$. Each row of the matrix $k(X_*)^T (K + \sigma_{\text{grid}}^2 I)^{-1}$ is an approximation of the exponential kernel to the square at the appropriate location, as it is the response to a vector y that is zero at all but one point. Here, K is the exponential-to-square covariance function that is typically used in denoising algorithms whose hyperparameters are σ_f , σ_n and S_c . We rescale the inputs and outputs to have mean zero and variance $\sigma_f = 1$ over the training set. We then compute the characteristic length scale σ_l which allows for a different distance measure for each input dimension. It will determine the relevance of an input point (pixel): if the length scale has a very high value, the covariance will become almost independent of this input, and the model will ignore it. This is closely related to the idea of automatic relevance determination [35]. Thus, all points not embedded in a structure like the target pixel will be considered as noise with frequencies above the S_c threshold in the fit and therefore removed from the model. The recovered phase image will therefore be free of the twin image. The GP-TIE algorithm consists of the following steps:

For each frequency f_x, f_y :

- (a) The inputs are N images of intensity taken in Fourier space at different distances: $I(f_x, f_y, z_1), I(f_x, f_y, z_2), \dots, I(f_x, f_y, z_N)$ (the inputs are the Fourier transforms of the reconstructed intensity images).
- (b) Set the frequency $S_c = \gamma \pi \lambda (f_x^2 + f_y^2)$. In our model, the frequency is $f = \pi \lambda (f_x^2 + f_y^2)$. However,

in the interest of eliminating not only the noise created by the high frequencies whose intensity variations decrease along the optical axis (recovering fine details), but also the low frequency noise created by the reduced defocusing range used during the reconstruction of the intensity images, we multiplied f by a factor γ varying from 0.05 to 1.1. Because with equal spacing, there is a forced trade-off between the low frequency noise and the blur (induced by the dual image) created by the high frequencies. Thus, this factor allows to make a compromise between precision and noise filtering because with equal spacing, there is a forced trade-off between the low frequency noise and the blur (induced by the dual image) created by the high frequencies.

- (c) Initialize the hyperparameters $\sigma_f = 1$ and $\sigma_n = 10^{-9}$ which are updated for each frequency in the regression to remove the high-frequency components greater than the threshold frequency S_c .
- (d) Obtain the output by calculating $\frac{\partial I(f_x, f_y, z)}{\partial z}$ according to the equations below:

$$\frac{\partial I(f_x, f_y, z)}{\partial z} = \frac{\partial h(f_x, f_y, z)}{\partial z} * I_{mn} \quad (12)$$

$$I_{mn} = I(f_x, f_y, z_1), I(f_x, f_y, z_2), \dots, I(f_x, f_y, z_N) \quad (13)$$

The vector I_{mn} is known from the Fourier transform of the reconstructed intensity images and

$$\begin{aligned} \frac{\partial h(f_x, f_y, z)}{\partial z} = & \left[\frac{\sigma_f^2}{\sigma_l^2} (z - z_1) \exp \left[-\frac{1}{\sigma_l^2} (z - z_1)^2 \right], \dots, \right. \\ & \left. - \frac{\sigma_f^2}{\sigma_l^2} (z - z_N) \exp \left[-\frac{1}{\sigma_l^2} (z - z_N)^2 \right] \right] \\ & \cdot [K(Z, Z) + \sigma_n I]^{-1} \end{aligned} \quad (14)$$

where $K(Z, Z)$ is the covariance matrix and σ_n is the variance of the additive Gaussian noise in the output. The vector $\frac{\partial h(f_x, f_y, z)}{\partial z}$ may be derived from the Gaussian Process (GP) regression with already known hyperparameters. Therefore, $\frac{\partial I(f_x, f_y, z)}{\partial z}$ at $z = 0$ (at the focal plane), is estimated by performing a GP regression on the data points $I(f_x, f_y, z_1), I(f_x, f_y, z_2), \dots, I(f_x, f_y, z_N)$. By repeating process, we obtain all the frequency components for the first derivative of the intensity spectrum at $z = 0$ [17]. The phase is then recovered using Equation (10). Note that, to increase the computational speed, all frequency components with the same values will share the same hyperparameters and therefore the same $\frac{\partial h(f_x, f_y, z)}{\partial z}$.

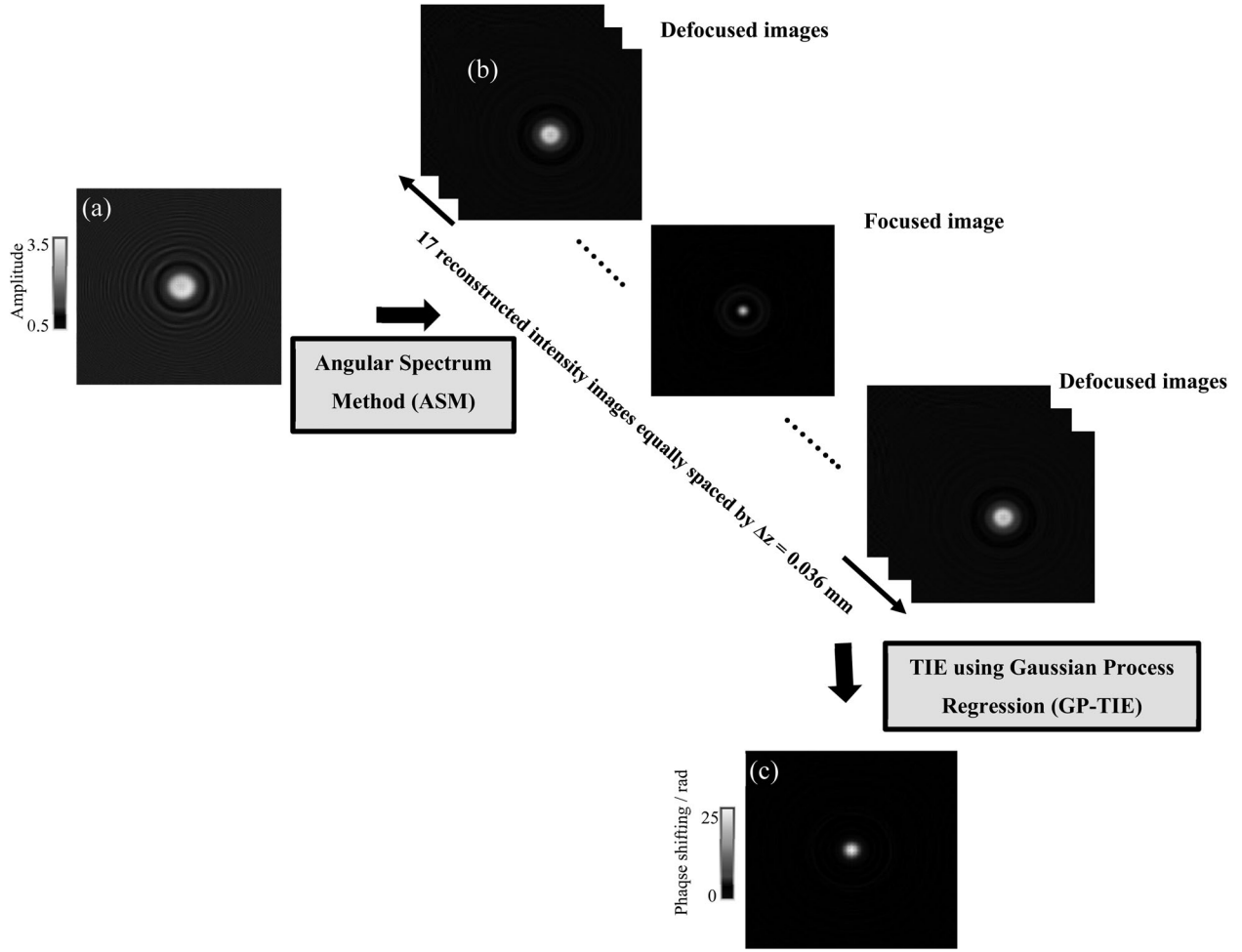


Figure 2. Phase image reconstruction from a stack of intensity images of a single hologram measured by a simulated microbeam of $10\ \mu\text{m}$ diameter by coupling the angular spectrum method and that of the TIE using Gaussian process regression (GP-TIE). (a) Normalized hologram of the simulated microbead, (b) dataset of intensity images digitally reconstructed at equal pitch $\Delta z = 0.036\text{mm}$ along the z propagation axis by the angular spectrum method, (c) image phase recovered by GP-TIE.

4. Results and discussion

4.1. Analysis of the simulation

We first tested our approach with a simulated microbead hologram with a maximum phase shift of $\Delta\varphi = 4.045 \times 2\pi$ (25.40 radians). The microbead is supposed to be entirely transparent. The process is illustrated in Figure 1. In the simulation, we used an illumination wavelength of $632.8\ \text{nm}$, and a hologram size of 500×500 pixels with a pixel size of $2.2\ \mu\text{m} \times 2.2\ \mu\text{m}$. The recording distance of the hologram was $5\ \text{cm}$ from the point source. Note that mathematically, a disk is more practical representation of a microbead because it is self-aligning [25]. We then reconstructed a stack of 17 intensity images at equal steps of $\Delta z = 0.036\ \text{mm}$ (same that of Zhong et al. [17]), over a defocus range ($13.8\text{--}14.2\ \text{mm}$) from the simulated microbead hologram using Equation (4) (Figure 2(b)). The dataset of reconstructed intensity images was used

to recover the phase by the GP-TIE method described in the previous section (Figure 2(c)).

To quantitatively evaluate the quality of the reconstructed image, the structural similarity index (SSIM) between the original phase object and the image obtained by the proposed method is calculated. The formula for SSIM is expressed as follows:

$$\text{SSIM}(I_1, I_2) = \frac{[2\mu_1\mu_2 + c_1][2\sigma_{1,2} + c_2]}{[\mu_1^2 + \mu_2^2 + c_1][\sigma_1^2 + \sigma_2^2 + c_2]} \quad (15)$$

where μ_1 is the average of I_1 , μ_2 is the average of I_2 , σ_1^2 is the variance of I_1 , σ_2^2 is the variance of I_2 , $\sigma_{1,2}$ is the cross-covariance of I_1 , and I_2 , The stabilization constants (c_1 , c_2) prevent division by a small denominator and can be selected as $c_1 = (k_1 L)^2$ and $c_2 = (k_2 L)^2$, where L is the dynamic range of the image and k_1, k_2 are both much smaller than 1. SSIM index between two images

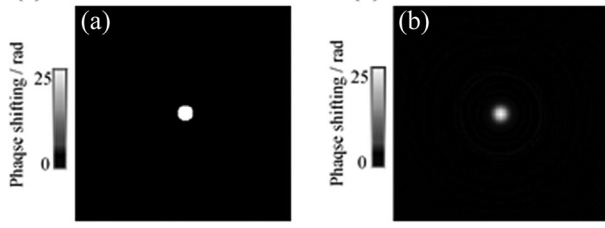


Figure 3. Comparison of the actual phase of the simulated microbead and the recovered phase (a) actual phase, (b) recovered phase (radians) by the proposed method.

ranges between 0 and 1 (the latter for identical images). The SSIM index defined above was: $SSIM = 0.915$. This clearly shows that the reconstructed image is quite like the original phase image of the simulated microbead. Figure 3(a,b) shows respectively, the original phase image of the simulated microbead and the reconstructed one.

4.2. Experimental data results

To apply our method to experimental holograms, we used a $10.00 \mu\text{m}$ diameter carboxylate microbeads whose hologram was acquired using the in-line holographic imaging device in Figure 1. The intensity image dataset reconstructed from the complex wave field using Equation (4), included 17 microbead intensity images. These different intensity planes were spaced by a pitch of $\Delta z = 0.036 \text{ mm}$ as used by Zhong et al. [17], over a defocus range (13.8–14 mm). The pitch was chosen to reduce the number of intensity images needed to recover the phase as described in [17]. For proposes of comparison, we also reconstructed the phase image directly from the digital hologram using an iterative reconstruction phase described in [4]. Figure 4(b,c) respectively shows the phase distribution reconstructed directly from the digital hologram and by our approach.

We used parameters such as: uniformity, entropy, standard deviation, and smoothness to quantitatively evaluate the image quality of the reconstructed microbeads (see Table 1). The formulas for parameters are expressed as follows:

$$\text{Standart deviation: } \sigma = \sqrt{\mu} = \sqrt{\sigma^2} \quad (16)$$

$$\text{Smoothness : } R = 1 - \frac{1}{1 + \sigma^2} \quad (17)$$

$$\text{Uniformity : } U = \sum_{i=0}^{L-1} \rho^2(z_i) \quad (18)$$

$$\text{Entropy : } e = - \sum_{i=0}^{L-1} \rho \log_2 \rho(z_i) \quad (19)$$

Table 1. Comparison of statistical parameter values for our approach output images obtained from a single hologram against iterative phase retrieval result.

	σ	R	U	e
Phase image reconstructed directly from hologram by iterative method	17.1932	0.0091	0.0896	29.5789
Phase image reconstructed from data multiple intensity images	12.3704	0.0047	0.6326	17.1188

where σ^2 is the variance, z_i is a random variable indicating intensity, $\rho(z)$ is the histogram of the intensity levels in a region, L the number of possible intensity levels.

The table compares the parameter values for each of the subimages outlined by the red boxes in Figure 4(b,c). The entropy and the standard deviation of the subimage of Figure 4(b) are higher than those of the subimage of Figure 4(c). This can be explained by the fact that the pixel values in the subimage of Figure 4(b) are more random than the pixel values of the others subimage of Figure 4(c). On the other hand, the subimage of Figure 4(b) is the least smooth and the least uniform as indicated by the smoothness values and the measure of uniformity. These calculated parameters show that the phase distribution reconstructed directly from the hologram is noisy. This is due to the in-line geometry of the experimental set-up and to the loss of phase information due to the detector's inability to register the phase. However, reconstruction using our approach achieves phase recovery with high resolution and less noise. In Figure 4(c), the noise of the twin image is almost completely cleaned up and the target is correctly reconstructed. The low presence of the observed twin image could be explained by the fact that the reconstructed image of the microbead does not appear at the exact distance where it was recorded during the experiment but at a distance L_r calculated by Equation (9). This can be a problem when reconstructing an experimental hologram, where the exact position of the object is not known. It is worth noting that in this digital reconstruction, all the microbeads are not the same plane; therefore, the reconstructions do not give an image with all the microbeads in focus. The microbead at the far left of the hologram (Figure 4(c)) is defocused because the reconstruction distance obtained by Equation (8) does not match the recording distance.

For the qualitative assessment, Figure 5 shows the intensity profiles along the blue line passing through the centre of one of the microbeads reconstructed by the iterative reconstruction method and our approach. In Figure 5(b) we can see outside the support of the

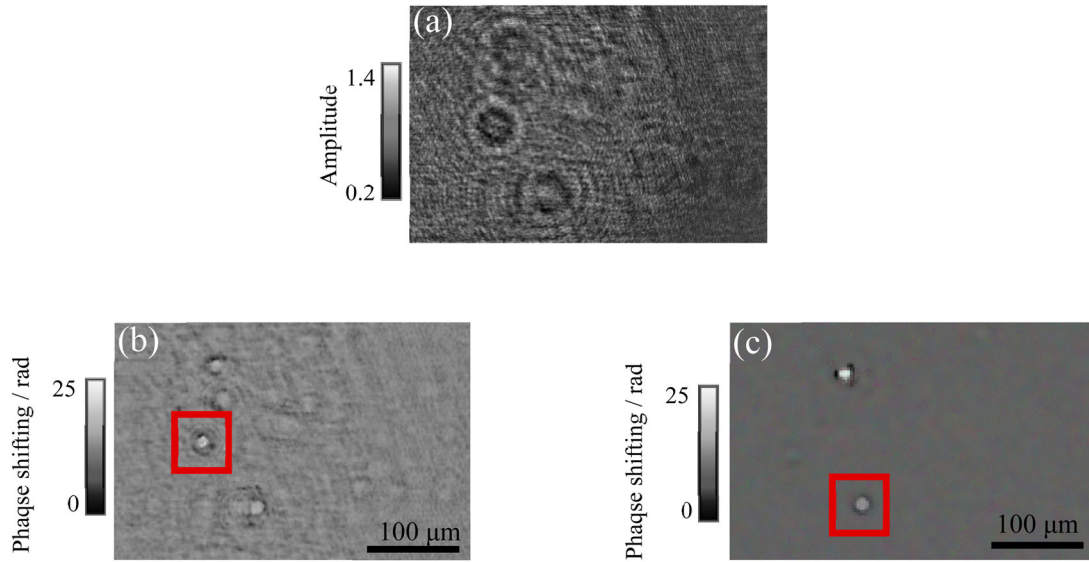


Figure 4. experimental and reconstructed hologram of a microbead using different reconstruction algorithms. (a) normalized hologram, (b) phase image obtained from hologram directly by conventional reconstruction at the object plane, (c) phase distribution obtained by our proposed method.

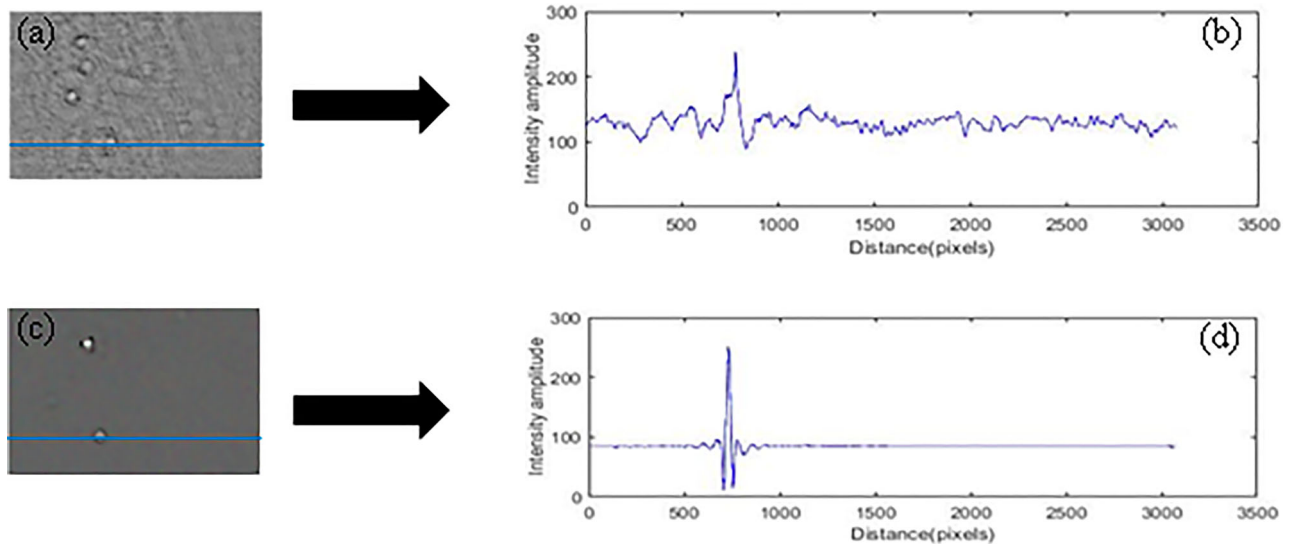


Figure 5. In front of each reconstruction, the intensity distribution along the horizontal line (in a and c) is displayed.

object, several oscillations. These oscillations are caused by the presence of twin images in the phase images reconstructed by the iterative reconstruction method. The one shown in Figure 5(d) gives a focused image of the microbead without a spurious twin image. The qualitative evaluation through intensity profiles clearly demonstrates that the proposed approach accurately recovers the phase information lost during the recording of the hologram (effectively suppresses the double image).

5. Conclusions

We have presented a new method to effectiveness recover the phase distribution of microbeads, devoid of noise due

to the twin image from a single in-line hologram, by combining the angular spectrum method and that of TIE using Gaussian process regression (GP-TIE). Numerical simulations and experimental results have verified the effectiveness and validity of the method. This proves that by using intensity images reconstructed from a single in-line holographic measurement, phase images with minimal noise can be obtained. The numerical calculations implemented in this new approach are simple with a fast-computing time. No object's surrounding and the use of multiple holograms is not necessary to accurately recover the phase image, as in most techniques used in in-line holography using a single hologram. The proposed technique can be applied to homogeneous biological

samples. However, for the method to work, the sample must be a pure phase object, allowing a linear deconvolution to be applied.

Disclosure statement

No potential conflict of interest was reported by the author(s).

Funding

This work was financially supported by SIDA (the Swedish International Development Cooperation Agency) through ISP (the International Science Program, Uppsala University).

References

- [1] Waller L, Tian L, Barbastathis G. Transport of intensity phase-amplitude imaging with higher order intensity derivatives. *Opt Express*. 2010;18(12):12552–12561.
- [2] Gerchberg RW, Saxton WO. Practical algorithm for the determination of phase from image and diffraction plane pictures. *Opt*. 1972;35(2):237–250.
- [3] Fienup JR. Reconstruction of an object from the modulus. *Opt Lett*. 1978;3(1):27–29.
- [4] Latychevskaia T, Fink HW. Solution to the twin image problem in holography. *Phys Rev Lett*. 2007;98(23):1–4. DOI:10.1103/PhysRevLett.98.233901
- [5] Latychevskaia T, Fink H-W. Practical algorithms for simulation and reconstruction of digital in-line holograms. *Appl Opt*. 2015;54(9):2424–2434. DOI:10.1364/ao.54.002424
- [6] Zhang Y, Greenbaum A, Feizi A, et al. Wide-field imaging of pathology slides using lensfree on-chip microscopy. *Sci Transl Med*. 2015;6(267). DOI:10.1364/CLEO_AT.2015.AW4J.6
- [7] Koren G, Polack F, Joyeux D. Twin-image elimination in in-line holography of finite-support complex objects. *Opt Lett*. 1991;16(24):1979. DOI:10.1364/ol.16.001979
- [8] Zhang Y, Pedrini G, Osten W, et al. Whole optical wave field reconstruction from double or multi in-line holograms by phase retrieval algorithm. *Opt Express*. 2003;11(24):3234. DOI:10.1364/OE.11.003234
- [9] Koren G, Polack F, Joyeux D. Iterative algorithms for twin-image elimination in in-line holography using finite-support constraints. *J Opt Soc Am A*. 1993;10(3):423. DOI:10.1364/josaa.10.000423
- [10] Mudanyali O, Tseng D, Oh C, et al. Compact, light-weight and cost-effective microscope based on lensless incoherent holography for telemedicine applications. *Lab Chip*. 2010;10(11):1417–1428. DOI:10.1039/c000453g
- [11] Rong L, Li Y, Liu S, et al. Iterative solution to twin image problem in in-line digital holography. *Opt Lasers Eng*. 2013;51(5):553–559. DOI:10.1016/j.optlaseng.2012.12.007
- [12] Greenbaum A, Sikora U, Ozcan A. Field-portable wide-field microscopy of dense samples using multi-height pixel super-resolution based lensfree imaging. *Lab Chip*. 2012;12(7):1242–1245. DOI:10.1039/c2lc21072j
- [13] McLeod E, Ozcan A. Microscopy without lenses. *Phys Today*. 2017;70(9):51–56. DOI:10.1063/PT.3.3693
- [14] Zhang Y, Pedrini G, Osten W, et al. Reconstruction of in-line digital holograms from two intensity measurements. *Opt Lett*. 2004;29(15):1787. DOI:10.1364/ol.29.001787
- [15] Reed Teague M. Deterministic phase retrieval: a Green's function solution. *J Opt Soc Am*. 1983;73(11):1434.
- [16] Streibl N. Phase imaging by the transport equation of intensity. *Opt Commun*. 1984;49(1):6–10. DOI:10.1016/0030-4018(84)90079-8
- [17] Jingshan Z, Claus RA, Dauwels J, et al. Transport of intensity phase imaging by intensity spectrum fitting of exponentially spaced defocus planes. *Opt Express*. 2014;22(9):10661. DOI:10.1364/oe.22.010661
- [18] Paganin D, Nugent KA. Noninterferometric phase imaging with partially coherent light. *Phys Rev Lett*. 1998;80(12):2586–2589. DOI:10.1103/PhysRevLett.80.2586
- [19] Gureyev TE, Roberts A, Nugent KA. Phase retrieval with the transport-of-intensity equation: matrix solution with use of Zernike polynomials. *J Opt Soc Am A*. 1995;12(9):1932. DOI:10.1364/josaa.12.001932
- [20] Allen LJ, Oxley MP. Phase retrieval from series of images obtained by defocus variation. *Opt Commun*. 2001;199:65–75.
- [21] Soto M, Acosta E. Improved phase imaging from intensity measurements in multiple planes. *Appl Opt*. 2007;46(33):7978–7981.
- [22] Guigay JP, Langer M, Boistel R, et al. Mixed transfer function and transport of intensity approach for phase retrieval in the Fresnel region. *Opt Lett*. 2007;32(12):1617–1619.
- [23] Snigirev A, Snigireva I, Kohn V, et al. On the possibilities of xray phase contrast microimaging by coherent high energy synchrotron radiation. *Rev Sci Instrum*. 1995;5486. DOI:10.1063/1.1146073
- [24] Sollich P. Edinburgh research explorer using the equivalent kernel to understand Gaussian process regression using the equivalent kernel to understand Gaussian process regression; 2004.
- [25] Sommargren GE, Weaver HJ. Diffraction of light by an opaque sphere. 1: description and properties of the diffraction pattern. *Appl Opt*. 1990;29(31):4646–4657.
- [26] Poon T-C, Liu J-P. Introduction to modern digital holography – index. Vol. Index, no. September; 2015.
- [27] Waller L, Luo Y, Yang SY, et al. Transport of intensity phase imaging in a volume holographic microscope. *Opt Lett*. 2010;35(17):2961–2963.
- [28] Zuo C, Chen Q, Qu W, et al. Noninterferometric single-shot quantitative phase microscopy. *Opt Lett*. 2013;38(18):3538–3541.
- [29] Zhou W-j, Guan X, Liu F, et al. Phase retrieval based on transport of intensity and digital holography. *Appl Opt*. 2018;57(1):229–234.
- [30] Latychevskaia T, Fink H-W. Simultaneous reconstruction of phase and amplitude contrast from a single holographic record. *Opt Exp*. 2009;17(13):10697–10705.
- [31] Montpellier DELUDE. Holographie numérique appliquée à l'imagerie 3D rapide de la circulation sanguine chez le poisson-zèbre Alexey Brodoline To cite this version: HAL Id: tel-02138965 Holographie numérique appliquée à l'imagerie 3D rapide de la circulation sanguine chez le poisson-zèbre Présentée par Alexey Brodoline; 2019.

- [32] Mudanyali O, Oztoprak C, Tseng D, et al. Detection of waterborne parasites using field-portable and cost-effective lensfree microscopy. *Lab Chip*. 2010;10(18): 2419–2423. DOI:[10.1039/c004829a](https://doi.org/10.1039/c004829a)
- [33] Kirchmann CC, Lundin E, Andr J. A study of digital in-line holographic microscopy for malaria detection; 2014.
- [34] Ayoub A, Tökés S, Orzó L, et al. A simple in-line digital holographic microscope; 2006.
- [35] Neal RM. Bayesian learning for neural networks. New York: Springer; 1996.
- [36] Litychevskaya T. Iterative phase retrieval for digital holography: tutorial. *J Opt Soc Am A*. 2019; 36:D31–D40.